Molecular surface coating of high-voltage cathodes in LPSCl-based all-solid-state lithium metal batteries

Alexander C. Forster[a], Jinsong Zhang[b], Laras Fadillah[a], Leonie Braks[a], Tingting Fu[c], Mario El Kazzi[b], Jang Wook Choi[d], and Ali Coskun*[a]*

[a]Department of Chemistry, University of Fribourg, Chemin de Musee 9, Fribourg 1700, Switzerland

[b] Paul Scherrer Institute, Electrochemistry Laboratory, Villigen 5232, Switzerland

[c]Laboratory of Advanced Technology, University of Geneva, 24 Quai Ernest-Ansermet Geneva 1204, Switzerland

[d]School of Chemical and Biological Engineering and Institute of Chemical Process, Seoul National University, 1 Gwanak-ro, Gwanak-gu, Seoul 08826, Republic of Korea

Corresponding Author

* Ali Coskun – Email: ali.coskun@unifr.ch

* Jang Wook Choi – Email: jangwookchoi@snu.ac.kr

ABSTRACT

Despite their improved safety, high energy density when paired with Li metal anode, all-solid-state batteries (ASSBs) continue to face significant challenges, notably the interface with the cathode active material (CAM), which is prone to both physical and (electro-)chemical degradation during cycling, especially when employing high-Ni CAMs. To address this issue, here, we introduced an organic surface anchoring strategy to stabilize the CAM surface and CAM-solid electrolyte interface using trifluoroacetamide (TFAA). A weak acid-base interaction between the CAM and TFAA creates a passivating layer, incorporating in-situ generated LiF, as a highly competitive alternative to conventional sol-gel-applied inorganic coating, i.e., $LiNbO_3$ (LNO). Comparative electrochemical and physico-chemical characterization of pristine, LNO-coated, and TFAA-coated NMC811 verified the efficiency of the organic anchoring strategy. Furthermore, we observed significant suppression in the formation of PO_x, SO_x, and P-S_n-P species, indicating efficient mitigation of the (electro-)chemical oxidation of LPSCl at the interface, thus enabling an improved capacity retention of 95% after 100 cycles at 0.1 C.

TOC GRAPHICS

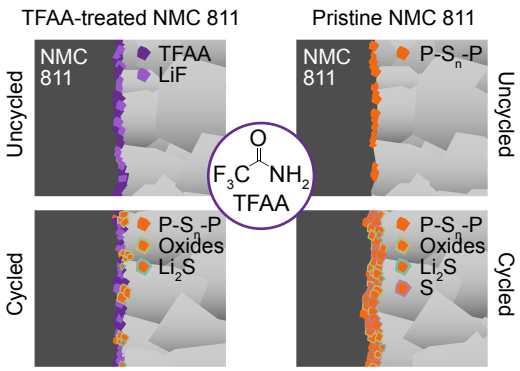

Since the discovery of lithium-ion batteries (LIBs) nearly 50 years ago[1], the development of LIBs as lightweight, high-energy density energy storage systems has revolutionized a wide range of applications, ranging from small portable electronics to electric vehicles (EVs).[2] Although the energy density of LIBs has gradually advanced over time, the increasing demand for batteries with higher energy densities has driven the LIB technology close to its theoretical limits. A key advancement to overcome these limitations is replacing the traditional graphite anode with lithium metal[3, 4], which increases the theoretical specific capacity from 350 to 3860 mAh g^{-1}. However, the low thermodynamic stability of conventional liquid electrolytes with lithium metal leads to significant parasitic reactions, unstable interface formation, and dendrite growth [4]. In this direction, an alternative approach is to replace liquid electrolytes with solid electrolytes to create all-solid-state lithium metal batteries (ASSLMBs).[5-8] Li_6PS_5Cl (LPSCl) stands out as a promising solid electrolyte (SE) with excellent ionic conductivity (> 1 mS cm^{-1}) and favorable ductility. Despite these advantages, LPSCl suffers from limited chemical stability and a narrow electrochemical window (2.1–2.3 V)[9], making it prone to degradation during processing and cycling at both the anode and cathode interfaces[10-15] (Figure 1). The degradation of LPSCl at the cathode active material (CAM) interface leads to the formation of phosphides, polysulfides, sulfates, sulfites, lithium sulfide, and elemental sulfur. Phosphates, sulfates, and sulfides are all by-products of the oxidation reaction of SE with the oxygen slowly released during cycling from the high-Ni CAM, , as observed by Ahaliabadeh *et al*.[16] through X-ray photoelectron spectroscopy (XPS) and time-of-flight secondary ion mass spectrometry (TOF-SIMS) measurements of the CAM interface. Furthermore, recent X-ray absorption spectroscopy (XAS) analysis of CAM interface by *Lellote et al*. demonstrated that the surface of the CAM also suffers from detrimental structural degradation, leading to the formation of inactive reduced transition metals, strongly contributing to the impedance rise.[17] Numerous efforts have been made to enhance the stability of the SE and catholyte by modifying their chemical structures or by incorporating additives or artificial interfaces.[18, 19] However, such modifications are often elaborate and can lead to reduced ionic conductivity or compromised physical properties. For SE in the cathode, maintaining high

ionic conductivity is crucial, as it improves accessibility to the CAM and reduces the internal resistance of the cathode.[20] An alternative approach involves optimizing the cathode interface between the CAM and SE by creating an artificial cathode electrolyte interface, CEI. This strategy is advantageous because it involves coating the CAM particles with only thin layers, protecting the CAM surface, preserving the bulk conductivity of the electrolyte, and the capacity of the CAM, thereby enhancing cathode performance. Typical inorganic CAM coatings developed for ASSB are LNO[21], Li-doped ZnO[22], Li_3YCl_6[23], boron-based species[24], and many more.

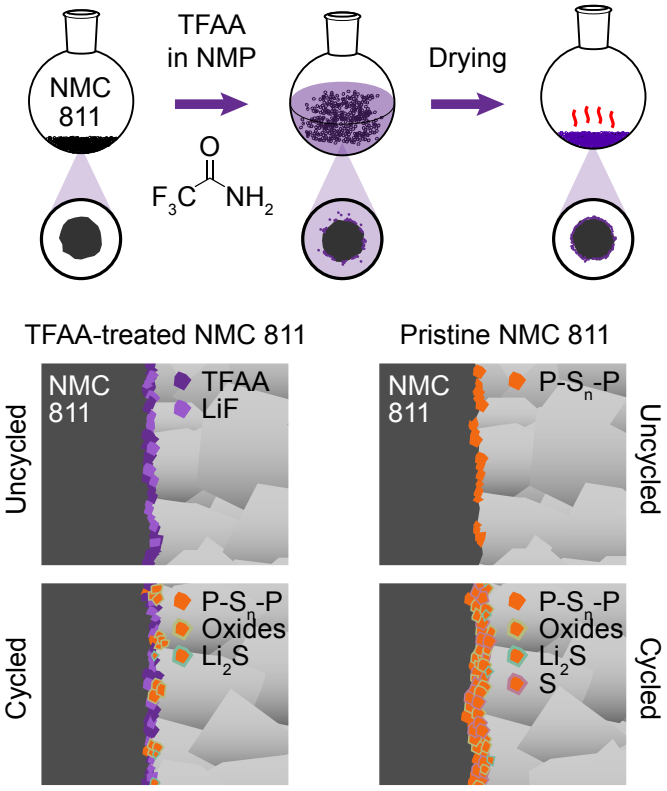

Figure 1. Schematic representation of organic cathode coating strategy (top) and interfacial degradation (bottom). On the left side, the TFAA additive partially decomposes into LiF on the surface of NMC, and upon cycling, forms only small amounts of polysulfides (P-S_n-P), oxides (SO_x, PO_x), and lithium sulfide (Li_2S). On the right side, the pristine NMC instantly forms polysulfides. Once cycled, large quantities of oxides, lithium sulfide, and sulfur are formed.

In this direction, we seek to enhance chemical stability at the cathode interface and within the cathode itself by introducing a more versatile CEI. This is achieved by employing an organic surface coating (2

wt% to NMC 811), trifluoroacetamide (TFAA) that in situ forms a thin, robust CEI, composed of decayed and actively attached TFAA on the NMC 811's surface, thus significantly enhancing interfacial stability and cycling performance. We hypothesized that a weak soft acid would mildly interact with the soft alkaline surface of the NMC 811, creating a non-destructive coating. Further introducing a fluorinated group could allow for in situ C-F bond decay and LiF formation, which is an ideal CEI component with a wide redox stability window and high chemical stability.[25] To this end, TFAA emerged as an ideal soft acid, which is significantly less acidic than carboxylic acids and is readily available. Additionally, the amide moiety of TFAA also provided efficient anchoring onto the basic surface of NMC811, thereby enhancing interfacial compatibility. Varying percentages (1, 2, 5, and 10 wt%) of TFAA were applied to the cathode active material NMC 811 by dissolving corresponding amounts of TFAA in N-methyl-2-pyrrolidone (NMP) and adding NMC 811 into this solution. The solvent was then evaporated, and the powder dried under vacuum.

A series of analyses was carried out to characterize the coated CAM, including Fourier-transformed infrared spectroscopy (FTIR), X-ray photoelectron spectroscopy (XPS), and powder X-ray diffraction (PXRD) (Figure 2, Figures S2-S4). FTIR analysis was carried out on NMC811 coated with 10 wt% of TFAA, as the signal intensity at lower additive amounts was too weak to observe (Figure 2a). Pristine TFAA showed characteristic N-H stretching vibrations at 3'300 cm^{-1}, corresponding to previously observed literature values.[26] These vibrations were significantly suppressed and red-shifted, an indication of strong hydrogen bonding interactions, once applied to NMC 811 surface. Additionally, the C=O stretching band is also red-shifted to 1680 cm^{-1}, further pointing to the strong interaction between TFAA and the CAM surface.

The interaction between TFAA and NMC811 was further studied by performing FTIR analysis on the treated powder at different stages of the heating process (Figure 2b). The attenuation of C-F, C=O, and N-H stretching vibrations at 1150, 1680, and 3300 cm^{-1}, respectively, with increasing temperature demonstrates clearly the partial decay of TFAA (Figure S4). In particular, the complete disappearance of

the C–F vibration at 100 °C suggests higher reactivity of TFAA on the NMC811 surface (Figure S4d). A F 1s core level XPS spectrum was acquired to analyse the surface chemistry after a heat treatment at 160 °C (Figure 2d). The C-F bond of the -CF_3 moiety of TFAA is observed at 689 eV. Once coated onto the NMC 811, we observe a second peak at 685 eV, which corresponds to LiF. These results suggest the in-situ formation of a surface layer through the degradation of surface-adsorbed TFAA, which can chemically and electrochemically separate the CAM from the LPSCl catholyte, thus effectively mitigating LPSCl oxidation at the interface.

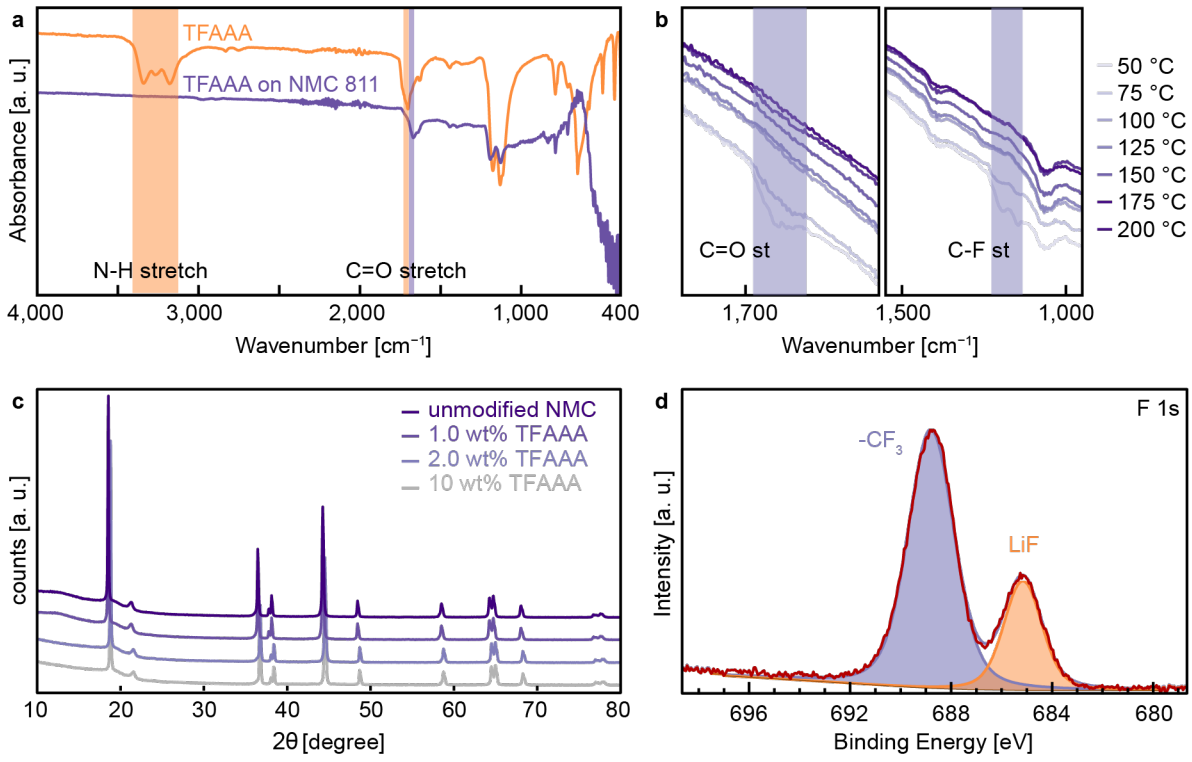

Figure 2. Spectral analysis of TFAA-coated NMC 811. a) FTIR spectra showing the difference between TFAA and NMC 811 powder with 10 wt% TFAA applied to its surface, b) FTIR spectra of 2wt% TFAA-treated NMC 811 in the region of C=O and C-F stretching vibrations after different temperature treatments at 50, 75, 100, 125, 150, 175, and 200 °C, c) PXRD diffractogram of increasing amounts of TFAA applied to NMC 811, d) Fitted F 1s core level XPS spectrum of 10 wt% TFAA applied to NMC 811.

The formation of LiF is attributed to the degradation of the trifluoromethyl group of surface–adsorbed TFAA during solvent at 160 °C. While LiF has a low Li-ion conductivity (6.0 μS cm^{-1})[27], it serves as a

highly effective interfacial layer owing to its high chemical stability and electrochemical window.[28] To probe the effect of TFAA on the crystallinity of NMC 811 particles, XRD analysis was performed (Figure 2c). The resulting spectrum of TFAA-coated NMC 811 overlays almost perfectly with the pristine one. This result suggests no significant change in the bulk crystallinity of NMC 811. Further, scanning electron microscopy with energy dispersive X-ray spectroscopy (SEM/EDX) analysis was performed on pristine and 10 wt% TFAA-coated NMC 811 particles (Figure S3). There was no discernible difference between the pristine and coated CAMs (2 and 10 wt% TFAA), further suggesting little to no change in the morphology of NMC 811 particles after the coating process. A detailed view of the NMC particle surface was obtained using scanning transmission electron microscopy coupled with electron energy loss spectroscopy (STEM-EELS) of both the TFAA-treated and untreated NMC 811 particles (Figure 3b and a). The elemental mapping reveals clear differences between the bare and TFAA-coated NMC811 particles. Both particles feature a homogeneous dispersion of Co and Mn across the particle surface. The untreated NMC particles, however, lack any F k-edge signal throughout the particle, while the TFAA-treated particles have a clearly localised F K-edge signal on the outermost nanometres, overlapping partially with the transition-metal distribution (Figure 3b). This result proves the homogeneous surface application of a fluorinated layer onto the NMC particles. The attenuation of the transition-metal Mn $L_{2,3}$-edge intensities near the surface further supports the presence of a coating that passivates the underlying oxide.

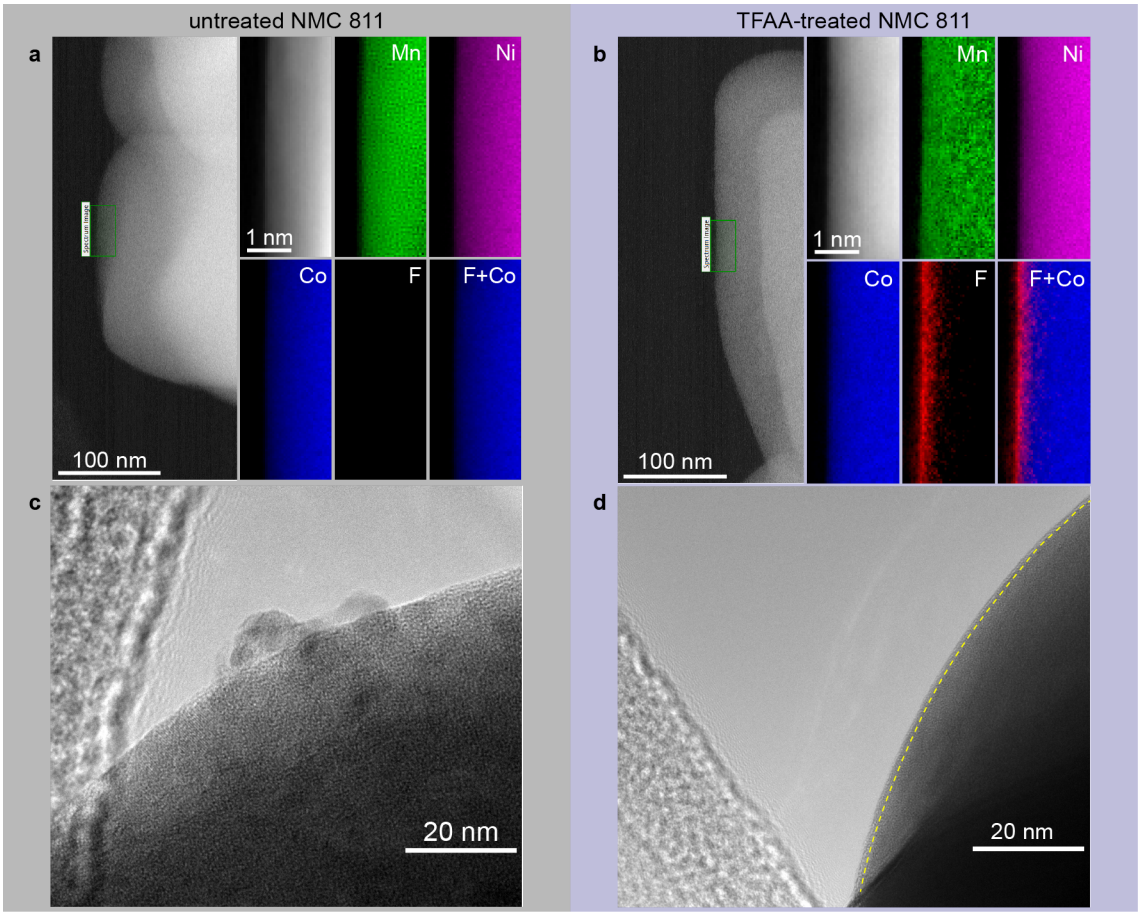

Figure 3. STEM–EELS elemental mapping and HRTEM of bare and TFAA-coated NMC811. a) and b) STEM–HAADF images and corresponding elemental maps for bare NMC811 (a) and TFAA-coated NMC811 (b). Uniform distributions of Ni, Mn, and Co across the particle surface are observed for both particles (pink, green and blue, respectively). Untreated NMC 811 (b) shows no discernible F signal (red), where the TFAA-coated NMC 811 displays a pronounced F K-edge signal concentrated near the surface, partially overlapping with the transition-metal signal, c) and d) HRTEM images of the NMC particle surfaces, untreated (c) and TFAA-treated (d). The TFAA-treated NMC particle exhibits a clear, thin interlayer on its surface.

High-resolution TEM (HRTEM) images further prove the amorphous nature of this 2-3 nm thick layer (Figure 3d), whereas the untreated NMC has well-defined edges (Figure 3c). The fine structure of the localised F K-edge signal in the EELS spectra and line scans (Figure S5) further suggests the presence of

metal-fluoride-like bonding. Li-F formation was not directly observed as the Li K-edge (55 eV) was not analysed due to significant overlap with the transition-metal M edges and the strong zero-loss tail, precluding reliable quantification. The formation of LiF was, however, further supported by the TOF-SIMS measurements performed on a cycled 2wt% TFAA-treated cathode (Figure S6). The depth profiling of the cathode clearly showed localised fluoride fragments at the surface of the cathode particles (Figure S6g), with the majority of these fragments being Li^+, Li_2^+, Li_2F^+, Li_2Cl^+, F^-, LiF_2^-, and CF_3^- as seen in the MS-spectra of the surface of a treated-NMC particle (Figure S6h-i).

Demonstrating the uniform coating across the NMC particle surface using STEM-EELS, the effect of the organic coating on the electrochemical performance was studied in the charge/discharge profiles using cyclic voltammetry (Figure 4a and 4b) with a lithium-indium-anode (30 : 70 at%) and 150 μm LPSCl separator in the voltage range of 1.88 and 3.68 V vs InLi/Li^+ at 150 MPa. 2 wt% of TFAA to NMC 811 was used for all experiments based on the EIS measurements before and after 10 cycles at 0.1 C, as it showed the lowest cathode resistance (Figure S7). The cathodes for all tests consisted of a 70 : 29 : 1 wt% mixture of NMC 811(+2 wt% TFAA) : LPSCl : C65. Cyclic voltammetry (CV) was performed on the cells at an applied pressure of 150 MPa. After each cycle, a potentiostatic impedance spectrum measurement (PEIS) was performed and is displayed below the corresponding CV graph (Figures 4c and 4d). For each cell, the 1st, 5th, 10th, 15th, 20th, and 25th cycles were displayed (in CV and EIS) in increasingly darker hues. The CV profile of the pristine cell (Figure 4a) changes drastically from the 1st to the 25th cycle, as evidenced by a significant decrease in peak intensity accompanied by a gradual shift in the peak positions. This is mainly attributed to CEI formation and interfacial reactions. Critically, the intensity change observed for pristine cathodes (Figure 4a) from the first to 25th cycle is more significant than for the 2 wt% TFAA-coated cathode (Figure 4b), which undergoes most of the changes during the first 5 cycles and stabilizes afterwards. The difference here is the rapid formation of CEI upon the application of TFAA, compared to the uncontrolled growth of CEI on pristine NMC 811, which continues to grow and thicken while reducing available capacity and increasing the cathode's inherent impedance (Figure

4c). In the CV profile, this increasingly thick CEI is evidenced by a shift in the H1→M peak in Figure 4a from 3.1 V in the first cycle to 3.4 V in the 25th cycle.[16, 29] Further studying the CV profiles after 10 to 25 cycles reveals that the TFAA additive retains more of the pristine charging structure, with characteristic peaks at 3.0, 3.1, 3.4, and 3.6 V (Figure 4b). This result further suggests a thin insulating CEI with little to no shifts to higher voltage present, proving the formation of a robust cathode interface.

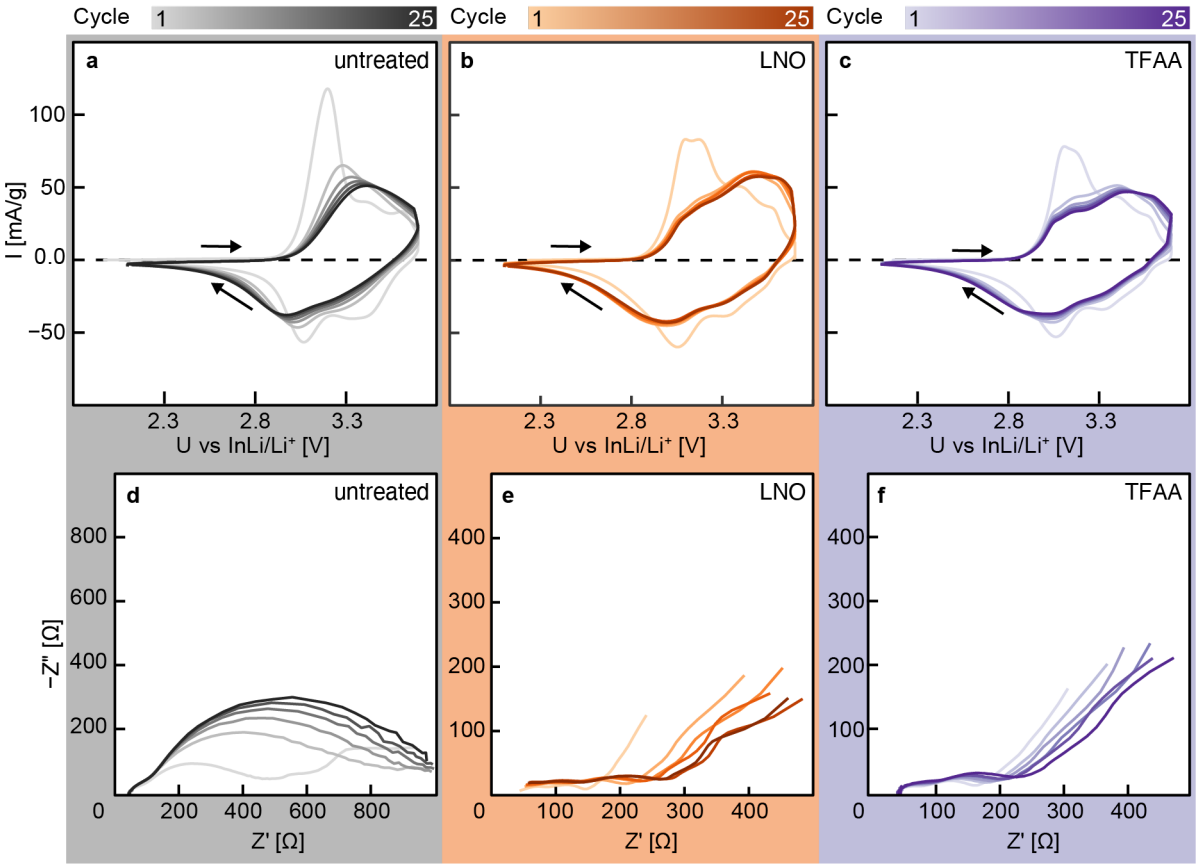

Figure 4. CV and EIS spectra of the first 25 cycles performed on LiIn – LPSCl – NMC-based cathodes with different NMC surface coatings. CV and Nyquist plots of (a, d) the untreated NMC 811, (b, e) the LNO-coated NMC 811, and (c, e) the 2wt% TFAA-treated NMC 811. For each cell, the cycles 1, 5, 10, 15, 20, and 25 are shown. The corresponding DRT spectra and circuit model, as well as the resistance growth by cycle, are shown in Figure S8.

To further understand the effect of TFAA coating on the NMC 811, PEIS analysis was performed during each cycle (charged state) and plotted for every 5th cycle (Figure 4c and 4d), showing a significant increase

in cathode resistance with increasing cycles for the pristine sample. The assignment of R_{CAT} and other resistances was confirmed using DRT calculations and modelling the expected circuit onto the obtained data (Figure S8). This trend clearly shows a growth in R_{CAT} while R_{SE} and others remain stable (Figure S8c). It should also be noted that while R_{CAT} increases for all cells, the most significant increase observed in the untreated cells surpasses that of the 2wt% coated cathode. This increase in resistance and difference between the coated and non-coated is most obvious when studying the initial impedance recorded after the first charging step, which is much larger for the pristine cell (Figure 4c) compared to the TFAA-coated one (Figure 4d). In comparison, the LNO-coated NMC 811 exhibits a lower initial resistance; however, the progressive increase (Figure S8d) indicates that its resistance continues to grow without stabilization, unlike the TFAA-treated sample. This suggests that although the inherently conductive LNO layer (5–10 nm) facilitates a low initial interfacial resistance, the continued formation of the CEI and associated parasitic by-products ultimately hinder the cathode's long-term electrochemical performance. To understand the influence of the coating on the deintercalation kinetics, GITT measurements were carried out for untreated, LNO-coated, and 2wt% TFAA-treated NMC 811-based half-cells (Figure S9). These measurements showed similar diffusion coefficients across the entire charge and discharge cycles (5.5 - 7.5 cm^2/s). This suggests that during the first cycle the TFAA-LiF-CEI does not interfere with the cathodes Li^+-ions diffusion into the NMC 811 particles.

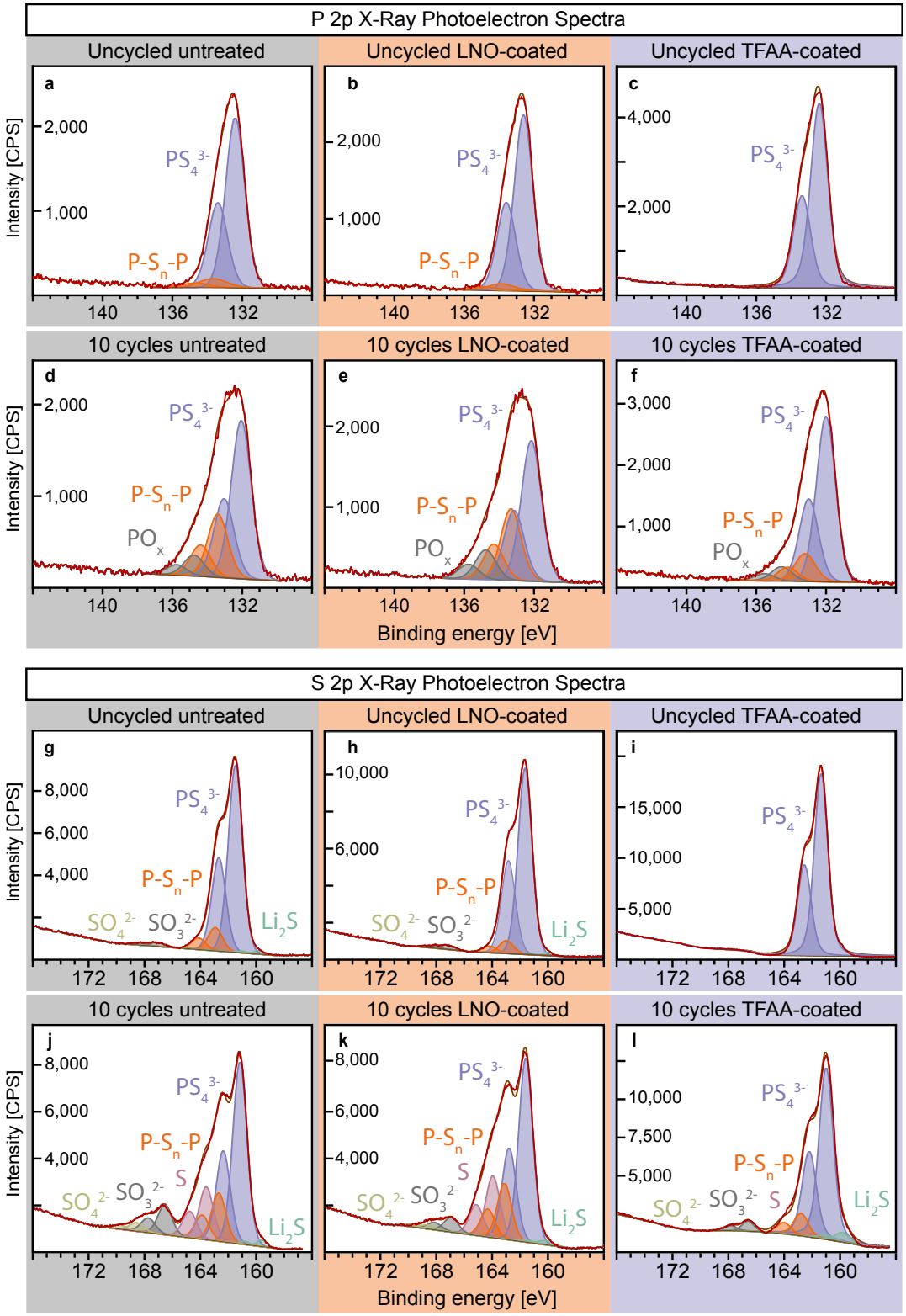

Figure 5. The deconvoluted P2p and S2p XPS spectra of the cathodes pre- and post-cycling (10 cycles). Grey shaded figures show the pristine, orange the 1 wt% LNO-coated, and purple the TFAA-coated NMC 811 cathodes. a–c) and g–i) show spectra of uncycled cells, while d–f) and j–l) show the same cells after 10 cycles at C/10. The arial proportions of the specific species are listed Table S1.

Considering the offset of the impedance spectra, we see that it remains the same for all cells at all cycles. This suggests no changes to the bulk electrolyte, allowing us to focus on the differences between the cathodes. The increase in impedance for the pristine cells is most noticeable within the first 5 cycles. There are, however, still significant impedance increases in the subsequent cycles and no apparent stagnation of this trend for the pristine cell. In the case of the TFAA-coated cell, we observe a drastically smaller increase, clearly pointing to the formation of an improved and more stable CEI. To understand the origin of differences in EIS and CV profiles for different electrolytes and the corresponding evolution of species during cycling, XPS measurements of the cells were performed before and after 10 cycles at C/10 (Figures S10-S15). Their relative proportions are listed in Table S1. In the analysis of the deconvoluted P 2p spectra of the LPSCl catholyte before (Figure 5a–c) and after cycling (Figure 5d–f), we can observe an immediate reaction between NMC 811 and LPSCl after mixing, except for the TFAA-coated CAM. This is apparent due to the formation of a new species, the polysulfide phase, not present for uncycled TFAA-coated NMC. This phase is destructive to the cathode performance, as it has a low ionic conductivity (1 – 100 nS/cm)[17, 30], and due to the high voltage operating window (1.88 to 3.68 V vs LiIn), it does not add to the reversible Li^+-storage capacity[31]. As discussed above, this phase is only observed for the pristine and LNO-coated CAMs and not for the TFAA-coated ones. Once cycled, we observe additional significant formation of Li_3PO_4 (grey), an oxidation product of LPSCl from the released oxygen from NMC 811 (6 and 14 mol% of PO_4^{3-} for pristine and LNO-coated NMC). These species have a significantly lower ionic conductivity (0.04 μS cm^{-1})[32] than pristine LPSCl (2.88 mS cm^{-1}) (Figure S1). Notably, they are far less present within the TFAA-coated CAM (5 mol%), suggesting suppressed side reactions between the NMC 811 and LPSCl catholyte. The same trend of reduced LPSCl decay is observed for the polysulfide species ($P–S_n–$

P, orange), which are also less present in the cycled TFAA-coated CAM compared to the pristine and LNO-coated ones. Further studying the interface, S 2p spectra were also analyzed (Figure 4g–l). Analogous to the P 2p spectra (Figure 5a–c), we observe a decay before cycling the cells (Figure 5g–i) for LNO- (28 mol% byproducts) and pristine cells (21 mol% byproducts), but no decay for the TFAA-coated ones (0 mol% byproducts). We observed the formation of small amounts of lithium sulfide (Li_2S, green). This is the only species found in higher concentration within the TFAA-coated cell (4 mol%) than in the pristine (0 mol%) or LNO-coated cells (1 mol%). along with new species that have also been observed previously.[17] Among these species, we observe SO_4^{2-} (beige) and SO_3^{2-} (grey), which are again the byproducts of oxygen released by NMC 811. These species greatly impede the function of the cathode as they not only have a low ionic conductivity but also a low electrical conductivity. This decreases the contact within the cathode to a large amount of the CAM and results in a significant capacity loss. These species are considerably greater for pristine and LNO-coated cathodes compared to the TFAA-coated one, which clearly shows lower amounts of these species. Finally, there are also high amounts of elemental sulfur (S, red) formed, which, while it is also of interest for Li^+-storage, does not reach the necessary low potential (below 1.5 V vs LiIn) in these cells for its utilization. Our results show no elemental sulfur within the TFAA-coated cathode, in good agreement with the low impedance increase observed for these cathodes in the EIS measurements (Figure 4). The pristine and LNO-coated cells show high levels of elemental sulfur.

To demonstrate the impact of the TFAA coating on the cycling behaviour, we compared the cycling performance of the pristine and TFAA-coated NMC 811 at C/10 between 1.88 and 3.68 V at 150 MPa of pressure (Figure 6). The cycling data shows a stable cycling behaviour with 2 wt% of TFAA on NMC 811, especially when compared to the pristine cell, which continues to lose

capacity after the 25 initial CV cycles. This result supports our hypothesis of a stable CEI formation after applying. We can observe that the capacity only mildly fades from cycle 1 to cycle 100 as shown in Figure 6b and 6c, where the 2 wt% TFAA-coated cell proves significantly more stable with high capacity retention of 95% after 100 cycles as opposed to 78% capacity retention for the pristine one (Figure 6c), thus clearly demonstrating the potential of the organic coating strategy to stabilize the cathode-solid electrolyte interface in ASSBs. Beyond this, the soft short observed for the pristine cathode at cycle 60 demonstrates the chemical lability of the untreated system (see Figure 6c). The strategy proves to be more effective compared to the

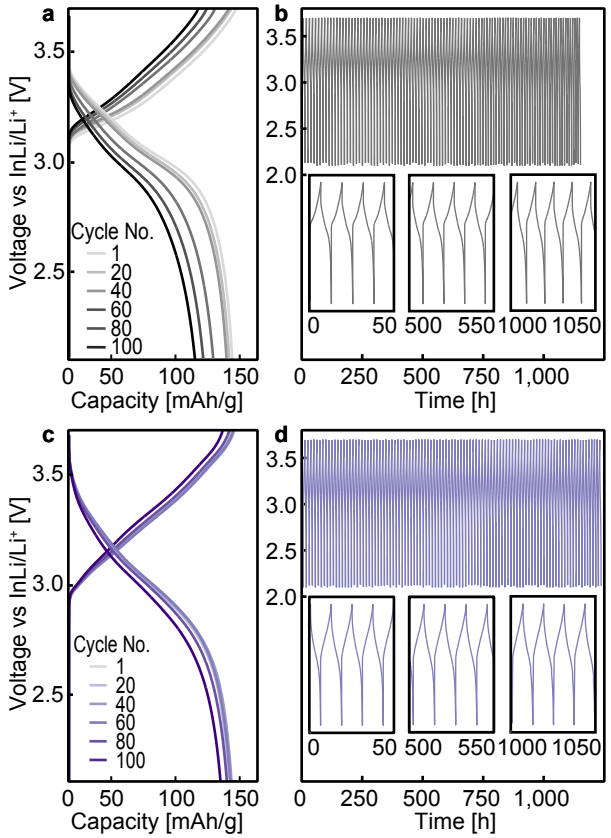

Figure 6. Cycling of the full cells after CV (from Figure 4). a) and c) Voltage over capacity plot for the cycles 1, 10, 20, 40, 60, 80, and 100 on the full cells with pristine NCM 811 and TFAA-

treated NMC 811, along with b) and d) Voltage over time profile with cut-outs at 0, 500, and 1000 h.

previously reported approaches in LIBs[33], which involved a prefabricated LiF layer. This is most likely due to the thick or non-uniform nature of such applications of artificial CEIs onto small particles. As we form the LiF layer in-situ and with only a small amount of organic molecules coated onto the cathode surface, we can circumvent these issues. Other examples achieved a similarly stable long-term capacity with other agyrodite-based electrolyte and catholytes, but with a large initial loss of capacity within the formation cycles.[34] Once again, the low additive amount of 2 wt% allows for stable cycling, demonstrating the potential of the organic coating strategy[35] to stabilize the interface between LPSCl and high-voltage cathodes.

In conclusion, this work demonstrates that TFAA surface treatment of NMC 811 cathodes results in a uniformly dispersed 2-3 nm thick TFAA-LiF layer on the NMC particles upon thermal treatment to 100 °C. This CEI significantly enhances interfacial stability in solid-state lithium metal batteries, effectively suppressing LPSCl electrolyte decomposition. The cells based on organic-coated NMC 811 show lower impedance and improved cycling stability when compared to untreated NMC 811 cathodes. These findings offer a facile strategy for mitigating chemical degradation at the cathode–electrolyte interface and underline the effectiveness of the organic coating strategy, supporting the development of more durable and commercially viable solid-state battery systems.

ASSOCIATED CONTENT

The supporting information is available free of charge at

Supporting Information: *Experimental details, EIS, XPS, and SEM images*.

AUTHOR INFORMATION

Corresponding Authors

Ali Coskun – Department of Chemistry, University of Fribourg, Fribourg 1700, Switzerland; orcid.org/0000- 0002-4760-1546;

Email: ali.coskun@unifr.ch

Jang Wook Choi – School of Chemical and Biological Engineering, Department of Materials Science and Engineering, and Institute of Chemical Processes, Seoul National University, Gwanak-gu, Seoul 08826, Republic of Korea; orcid.org/0000-0001-8783-0901;

Email: jangwookchoi@snu.ac.kr

Authors

Alexander C. Forster– Department of Chemistry, University of Fribourg, Chemin de Musee 9, Fribourg 1700, Switzerland

Jinsong Zhang – Paul Scherrer Institute, Electrochemistry Laboratory, Villigen 5232, Switzerland

Laras Fadillah - Department of Chemistry, University of Fribourg, Chemin de Musee 9, Fribourg 1700, Switzerland

Leonie Braks – Department of Chemistry, University of Fribourg, Chemin de Musee 9, Fribourg 1700, Switzerland

Tingting Fu - Laboratory of Advanced Technology, University of Geneva, Geneva 1204, Switzerland

Mario El Kazzi – Paul Scherrer Institute, Electrochemistry Laboratory, Villigen 5232, Switzerland

Notes

The authors declare no competing financial interest.

ACKNOWLEDGMENT

A.C., M.E.K., and J.W.C. acknowledge the support from the Swiss National Science Foundation (SNF) (Sinergia, CRSII5_202296).

REFERENCES

(1) Scrosati, B. History of lithium batteries. *Solid State Electrochem* **2011**, *15*, 1623-1630. DOI: https://doi.org/10.1007/s10008-011-1386-8.

(2) Goodenough, J. B.; Whittingham, M. S.; Yoshino, A. Lithium-Ion Batteries; The Royal Swedish Academy of Sciences: Stockholm, Sweden, **2019**.

(3) Zhao, Y.; Zhou, T.; Ashirov, T.; Kazzi, M. E.; Cancellieri, C.; Jeurgens, L. P. H.; Choi, J. W.; Coskun, A. Fluorinated ether electrolyte with controlled solvation structure for high voltage lithium metal batteries. *Nat. Commun.* **2022**, *13* (1), 2575. DOI: 10.1038/s41467-022-29199-3.

(4) Chen, Y.; Luo, Y.; Zhang, H.; Qu, C.; Zhang, H.; Li, X. The Challenge of Lithium Metal Anodes for Practical Applications. *Small Methods* **2019**, *3*, 1800551. DOI: 10.1002/smtd.201800551.

(5) Hatzell, K. B.; Chen, X. C.; Cobb, C. L.; Dasgupta, N. P.; Dixit, M. B.; Marbella, L. E.; McDowell, M. T.; Mukherjee, P. P.; Verma, A.; Viswanathan, V.; et al. Challenges in Lithium Metal Anodes for Solid-State Batteries. *ACS Energy Letters* **2020**, *5*, 922-934. DOI: 10.1021/acsenergylett.9b02668.

(6) Bachman, J. C.; Muy, S.; Grimaud, A.; Chang, H. H.; Pour, N.; Lux, S. F.; Paschos, O.; Maglia, F.; Lupart, S.; Lamp, P.; et al. Inorganic Solid-State Electrolytes for Lithium Batteries: Mechanisms and Properties Governing Ion Conduction. *Chem Rev* **2016**, *116*, 140-162. DOI: 10.1021/acs.chemrev.5b00563.

(7) Asano, T.; Sakai, A.; Ouchi, S.; Sakaida, M.; Miyazaki, A.; Hasegawa, S. Solid Halide Electrolytes with High Lithium-Ion Conductivity for Application in 4 V Class Bulk-Type All-Solid-State Batteries. *Adv. Mater.* **2018**, *30* (44), e1803075. DOI: 10.1002/adma.201803075.

(8) Li, F.; Cheng, X.; Lu, L. L.; Yin, Y. C.; Luo, J. D.; Lu, G.; Meng, Y. F.; Mo, H.; Tian, T.; Yang, J. T.; et al. Stable All-Solid-State Lithium Metal Batteries Enabled by Machine Learning Simulation Designed Halide Electrolytes. *Nano Lett.* **2022**, *22* (6), 2461-2469. DOI: 10.1021/acs.nanolett.2c00187.

(9) Xiao, Y.; Miara, L. J.; Wang, Y.; Ceder, G. Computational Screening of Cathode Coatings for Solid-State Batteries. *Joule* **2019**, *3* (5), 1252-1275. DOI: 10.1016/j.joule.2019.02.006.

(10) Otto, S. K.; Riegger, L. M.; Fuchs, T.; Kayser, S.; Schweitzer, P.; Burkhardt, S.; Henss, A.; Janek, J. In Situ Investigation of Lithium Metal–Solid Electrolyte Anode Interfaces with ToF-SIMS. *Advanced Materials Interfaces* **2022**, *9* (13), 2102387. DOI: 10.1002/admi.202102387.

(11) Riegger, L. M.; Schlem, R.; Sann, J.; Zeier, W. G.; Janek, J. Lithium-Metal Anode Instability of the Superionic Halide Solid Electrolytes and the Implications for Solid-State Batteries. *Angew. Chem. Int. Ed.* **2021**, *60*, 6718-6723. DOI: 10.1002/anie.202015238.

(12) Riegger, L. M.; Mittelsdorf, S.; Fuchs, T.; Rueß, R.; Richter, F. H.; Janek, J. Evolution of the Interphase between Argyrodite-Based Solid Electrolytes and the Lithium Metal Anode─The Kinetics of Solid Electrolyte Interphase Growth. *Chemistry of Materials* **2023**, *35* (13), 5091–5099. DOI: 10.1021/acs.chemmater.3c00676.

(13) Ji, X.; Li, S.; Cao, M.; Liang, R.; Xiao, L. L.; Yue, K.; Liu, S.; Zhou, X.; Guo, Z. H. Crosslinked Polymer-Brush Electrolytes: An Approach to Safe All-Solid-State Lithium Metal Batteries at Room Temperature. *Batteries & Supercaps* **2021**, *5* (2), e202100319. DOI: 10.1002/batt.202100319.

(14) Ko, S.; Obukata, T.; Shimada, T.; Takenaka, N.; Nakayama, M.; Yamada, A.; Yamada, Y. Electrode potential influences the reversibility of lithium-metal anodes. *Nature Energy* **2022**, 7, 1217–1224. DOI: 10.1038/s41560-022-01144-0.

(15) Ryu, H.-H.; Park, K.-J.; Yoon, C. S.; Sun, Y.-K. Capacity Fading of Ni-Rich Li[NixCoyMn1–x–y]O_2 ($0.6 \le x \le 0.95$) Cathodes for High-Energy-Density Lithium-Ion Batteries: Bulk or Surface Degradation? *Chem. Mater.* **2018**, *30* (3), 1155-1163. DOI: 10.1021/acs.chemmater.7b05269.

(16) Ahaliabadeh, Z.; Miikkulainen, V.; Mantymaki, M.; Mousavihashemi, S.; Lahtinen, J.; Lide, Y.; Jiang, H.; Mizohata, K.; Kankaanpaa, T.; Kallio, T. Understanding the Stabilizing Effects of Nanoscale Metal Oxide and Li-Metal Oxide Coatings on Lithium-Ion Battery Positive Electrode Materials. *ACS Appl. Mater. Interfaces* **2021**, *13* (36), 42773-42790. DOI: 10.1021/acsami.1c11165.

(17) Lelotte, B.; Vaz, C. A. F.; Xu, L.; Borca, C. N.; Huthwelker, T.; Pele, V.; Jordy, C.; Gubler, L.; El Kazzi, M. Spatio-Chemical Deconvolution of the $LiNi_{0.6}Co_{0.2}Mn_{0.2}O_2/Li_6PS_5Cl$ Interphase Layer in All-Solid-State Batteries Using Combined X-ray Spectroscopic Methods. *ACS Appl. Mater. Interfaces* **2025**, *17*, 14645-14659. DOI: 10.1021/acsami.4c19857.

(18) Muruganantham, R.; Wu, H.-W.; Lo, Y.; Liu, W.-R. Improving electrochemical stability by modifying the Li_6PS_5Cl entailed with the mixed phase of $Li_{6.4}La_3Zr_{1.4}Ta_{0.6}O_{12}$ composite solid electrolytes for all-solid-state lithium battery applications. *Surface and Coatings Technology* **2024**, *479*, 130480 . DOI: 10.1016/j.surfcoat.2024.130480.

(19) Indrawan, R. F.; Matsuda, R.; Hikima, K.; Matsuda, A. Enhanced electrochemistry stability of oxygen doped Li_6PS_5Cl argyrodite solid electrolyte by liquid-phase synthesis. *Solid State Ionics* **2023**, *401*, 116344. DOI: 10.1016/j.ssi.2023.116344.

(20) Orue, A.; López del Amo, J. M.; Aguesse, F.; Casas-Cabanas, M.; López-Aranguren, P. Concerted ionic-electronic conductivity enables high-rate capability Li-metal solid-state batteries. *Energy Storage Materials* **2023**, *54*, 524-532. DOI: 10.1016/j.ensm.2022.11.004.

(21) Morino, Y.; Shiota, A.; Kanada, S.; Bong, W. S. K.; Kawamoto, K.; Inda, Y.; Tsukasaki, H.; Mori, S.; Iriyama, Y. Design of Cathode Coating Using Niobate and Phosphate Hybrid Material for Sulfide-Based Solid-State Battery. *ACS Appl Mater Interfaces* **2023**, *15* (30), 36086-36095. DOI: 10.1021/acsami.3c02827.

(22) Kang, C.; Park, Y.; Kim, Y.; Kim, S. M.; Ha, S.; Yoon, H. G.; Oh, K. W.; Shin, K.-Y.; Kim, B. H. Solution-processed ZnO coated on LiNi0.8Mn0.1Co0.1O2(NMC811) for enhanced performance of Li-ion battery cathode. *Frontiers in Energy Research* **2023**, *11*, 1235721. DOI: 10.3389/fenrg.2023.1235721.

(23) Kim, J. S.; Jung, S.; Kwak, H.; Han, Y.; Kim, S.; Lim, J.; Lee, Y. M.; Jung, Y. S. Synergistic halide-sulfide hybrid solid electrolytes for Ni-rich cathodes design guided by digital twin for all-solid-State Li batteries. *Energy Storage Materials* **2023**, *55*, 193-204. DOI: 10.1016/j.ensm.2022.11.038.

(24) Skvortsova, I. A.; Orlova, E. D.; Boev, A. O.; Aksyonov, D. A.; Moiseev, I.; Pazhetnov, E. M.; Savina, A. A.; Abakumov, A. M. Comprehensive analysis of boron-induced modification in LiNi0.8Mn0.1Co0.1O2 positive electrode material for lithium-ion batteries. *Journal of Power Sources* **2023**, *583*, 233571. DOI: 10.1016/j.jpowsour.2023.233571.

(25) Zhou, T.; Zhao, Y.; El Kazzi, M.; Choi, J. W.; Coskun, A. Stable Solid Electrolyte Interphase Formation Induced by Monoquat-Based Anchoring in Lithium Metal Batteries. *ACS Energy Letters* **2021**, *6* (5), 1711-1718. DOI: 10.1021/acsenergylett.1c00274.

(26) Sterkhova, I. V.; Astakhova, V. V.; Shainyan, B. A. X-ray, FTIR and DFT study of new iodine-containing derivatives of trifluoroacetamide. *Journal of Molecular Structure* **2017**, *1141*, 351-356. DOI: 10.1016/j.molstruc.2017.03.095.

(27) Li, C.; Gu, L.; Maier, J. Enhancement of the Li Conductivity in LiF by Introducing Glass/Crystal Interfaces. *Advanced Functional Materials* **2012**, *22* (6), 1145-1149. DOI: 10.1002/adfm.201101798.

(28) Richards, W. D.; Miara, L. J.; Wang, Y.; Kim, J. C.; Ceder, G. Interface Stability in Solid-State Batteries. *Chemistry of Materials* **2015**, *28* (1), 266-273. DOI: 10.1021/acs.chemmater.5b04082.

(29) Li, X.; Liu, J.; Banis, M. N.; Lushington, A.; Li, R.; Cai, M.; Sun, X. Atomic layer deposition of solid-state electrolyte coated cathode materials with superior high-voltage cycling behavior for lithium ion battery application. *Energy Environ. Sci.* **2014**, *7* (2), 768-778. DOI: 10.1039/c3ee42704h.

(30) Li, X.; Sun, X.; Xiao, B.; Wang, D.; Liang, J. Inorganic Polysulfide Chemistries for Better Energy Storage Systems. *Acc. Chem. Res.* **2023**, *56* (24), 3547-3557. DOI: 10.1021/acs.accounts.3c00484.

(31) Lee, S.; Kim, T.-H.; Kim, K.; Song, G.; Park, J.; Lee, M.; Jung, H.; Park, K.; Choi, S. H.; Song, J.; Lee, K. T. Mechano-Electrochemical Healing at the Interphase Between $LiNi_{0.8}Co_{0.1}Mn_{0.1}O_2$ and Li_6PS_5Cl in All-Solid-State Batteries. *Adv. Energy Mater.* **2025**, *15*, 2405782. DOI:10.1002/aenm.202405782.

(32) Sun, Y.-Q.; Luo, X.-T.; Zhu, Y.-S.; Liao, X.-J.; Li, C.-J. Li_3PO_4 electrolyte of high conductivity for all-solid-state lithium battery prepared by plasma spray. *Journal of the European Ceramic Society* **2022**, *42*, 4239-4247. DOI: 10.1016/j.jeurceramsoc.2022.04.010.

(33) Llanos, P. S.; Ahaliabadeh, Z.; Miikkulainen, V.; Lahtinen, J.; Yao, L.; Jiang, H.; Kankaanpaa, T.; Kallio, T. M. High Voltage Cycling Stability of LiF-Coated NMC811 Electrode. *ACS Appl. Mater. Interfaces* **2024**, *16* (2), 2216-2230. DOI: 10.1021/acsami.3c14394.

(34) Liang, J.; Zhu, Y.; Li, X.; Luo, J.; Deng, S.; Zhao, Y.; Sun, Y.; Wu, D.; Hu, Y.; Li, W.; et al. A gradient oxy-thiophosphate-coated Ni-rich layered oxide cathode for stable all-solid-state Li-ion batteries. *Nat Commun* **2023**, *14*, 146. DOI: 10.1038/s41467-022-35667-7.

(35) Huang, Y.; Zhou, L.; Li, C.; Yu, Z.; Nazar, L. F. Waxing Bare High-Voltage Cathode Surfaces to Enable Sulfide Solid-State Batteries. *ACS Energy Letters* **2023**, *8* (11), 4949-4956. DOI: 10.1021/acsenergylett.3c01717.